Journal of Materials Chemistry A

ARTICLE

Ultrafine Co_3O_4 Nanoparticles-Engineered Binary Metal Nitride Nanorods with Interfacial Charge Redistribution for Enhanced Water Splitting

Received 00th January 20xx,
Accepted 00th January 20xx

DOI: 10.1039/x0xx00000x

www.rsc.org/

Dinh Chuong Nguyen,[a] Thi Luu Luyen Doan,[b] Xinfeng Zhu,[a] Nam Hoon Kim,[a*] Joong Hee Lee[a,b*]

Herein, an efficient bifunctional electrocatalyst based on binary metal nitride (Zn_3N_2-Co_2N) nanorod arrays decorated with ultrathin Co_3O_4 nanoparticles is prepared to improve overall water splitting performance. Notably, a charge redistribution process occurs at the heterointerface between the host metal nitride and the guest Co_3O_4, resulting in the regulation of both their electronic structures to facilitate the reaction kinetics of hydrogen/oxygen evolution reaction (HER/OER). Using the material to catalyze the HER, current density of 10 and 50 mA cm^{-2} are delivered at small overpotential of 80.5 and 121.7 mV, respectively. Similarly, for OER, under the action of the material, overpotential of only 271.7 and 335.7 mV, respectively, is required to achieve 10 and 50 mA cm^{-2}. Thus, an electrolyzer is assembled with the material as both cathode and anode, and shows high performance with a small cell voltage of 1.59 V at 10 mA cm^{-2}, and excellent stability.

Introduction

Hydrogen (H_2) as a promising alternative to traditional fossil fuel has attracted considerable attention, since the global energy crisis and environmental pollution associated with the widespread combustion of fossil fuel are radically increasing nowadays.[1–4] The production of H_2 based on electrochemical water splitting is considered an effective technique, both in terms of the environment, and the economy.[5–7] During water electrolysis, H_2 gas is produced at the cathodic electrode by an electrochemical reaction, namely the hydrogen evolution reaction (HER), while oxygen (O_2) gas is produced at the anodic electrode via another reaction, namely the oxygen evolution reaction (OER).[8–10] The sluggish kinetics of both HER and OER form the unavoidable bottleneck in water splitting, lowering its real performance well below that predicted in theory.[11,12] The previous studies demonstrated that integrating the noble metal-based electrocatalysts, such as Pt/C for HER and RuO_2 or IrO_2 for OER, to form an electrolyzer, can yield the expected water-splitting performance.[13–15] However, the scarcity and high cost of these noble metals make it difficult to commercialize the water electrolyzer.[16,17] Accordingly, exploring cost-effective, highly efficient, and stable bifunctional electrocatalysts for both HER and OER is a critical strategy to develop water splitting toward the large-scale industrial production of green H_2. Earth-abundant transition metal nitrides (TMNs), such as cobalt nitride (Co_2N) and zinc nitride (Zn_3N_2), have drawn much research attention as efficient bifunctional electrocatalysts for overall water splitting, on account of their advantages of metallic conductivity, high corrosion resistance, special electronic structure, and their multi-valence states.[18] Unfortunately, the single-phase nitrides still show unsatisfactory catalytic performance for HER and OER as compared to those of the noble metals-based electrocatalysts, causing the consumption of rather high electrical power to establish overall water splitting.[19] By combining two TMNs to form a binary nitride system, the catalytic activity can be significantly improved considering both the large inheritance from the merits of individual components, and the chemical coupling effects of these nitride components. For example, Chen et al. reported on the accurate activation of MoN catalyst for HER by incorporating Ni atoms, which resulted in the formation of Mo-Ni binary nitride.[20] The findings proved that after the introduction of Ni, the synthesized Mo-Ni binary nitride showed a proper bonding strength between Mo active site and the H intermediate, thus its HER catalytic activity was much better than that of the MoN alone. Furthermore, the Mo-Ni binary nitride outperformed the mono-metal nitride in terms of structural stability as well. Recently, the Guo group proposed the Mo_2N/Co_xN heterojunction nanosheets with interfacial electron redistribution as bifunctional electrocatalysts for overall water splitting.[21] The theoretical calculations demonstrated that the proposed Mo_2N/Co_xN had favorable

[a] Department of Nano Convergence Engineering, Jeonbuk National University, Jeonju, Jeonbuk, 54896, Republic of Korea.
[b] Division of Mechanical Design Engineering, School of Engineering, Jeonbuk National University, Jeollabuk-do Jeonju 54896, Republic of Korea.
[c] Carbon Composite Research Center, Department of Polymer-Nano Science and Technology, Jeonbuk National University, Jeonju, Jeonbuk, 54896, Republic of Korea.
* Corresponding authors: E-Mail: nhk@jbnu.ac.kr (Prof. N. H. Kim)
jhl@jbnu.ac.kr (Prof. J. H. Lee)
Fax: +82 63 270 2341; Tel: +82 63 270 2301.

† Electronic Supplementary Information (ESI) available. See DOI: 10.1039/x0xx00000x

water dissociation kinetics, which could be attributed to the electron redistribution at the heterointerface between Mo_2N and Co_xN. This, coupled with the structural advantages of large accessible surface and abundant pore exposure to enhance mass transport capability, endowed the Mo_2N/Co_xN with excellent electrocatalytic activity for both HER and OER. In addition to TMNs, transition metal oxides (TMOs), such as cobalt oxides (Co_3O_4), have also been widely employed for water-splitting electrocatalysts, owing to their loosely bonded d electrons.[22] The problem is that the electrical conductivity of cobalt oxides is rather poor, leading to the slow electron transfer to catalytically active sites and thereby an unsatisfactory electrocatalytic activity.[23] This drawback can be overcome by constructing a hybrid structure containing TMOs and conductive components because there are also synergistic effects. Liu et al. reported that in the $Co_3O_4@MoS_2$ heterostructure, strong electronic interaction between Co_3O_4 and MoS_2 components caused the charge redistribution, which resulted in a change in the Gibbs free energy of the reaction intermediates for significant improvement of overall water splitting performance.[24] Elsewhere, Zhou et al. demonstrated that the existence of electronic interactions between CuO_x and Co_3O_4 components in $CuO_x@Co_3O_4$ heterostructure led to improved electronic conductivity of the entire $CuO_x@Co_3O_4$ material.[25] Regarding hybrid structure of TMNs and TMOs, TMNs with their metallic highly electron conductive characteristic can promote electron transfer from the conductive support to the catalytic active sites,[26] while in the introduction of TMOs, the water dissociation can be expedited to boost the overall kinetics of water splitting.[27] It is well known that in addition to the optimization of adsorption/desorption energies of intermediates, the water dissociation must be focused to enhance the efficiency of overall water splitting.[28,29] Liu et al. proved that Co_3O_4 with the thermal equilibrium of OH adsorption on Co atoms promoted the break of the H–OH bond, and thus the incorporation of Co_3O_4 into host materials could provide active sites for adsorption of OH group that is beneficial for water dissociation.[24] Moreover, the presence of TMOs over the surface of other transition metal compounds can increase the adsorption of nearby H intermediates, which is conducive to the HER process.[30] It is also demonstrated that the hybrid structure of TMOs and TMNs can endow the catalyst with charge redistribution at the heterointerface between the components, also benefiting the intermediate adsorption, and thereby further enhancing the reaction kinetics of both HER and OER.[31] Liu et al. found that the heterostructure CoO_x/CoN_y nanoparticles was beneficial to the catalytic activity of the entire CoO_x/CoN_y embedded in carbon-nitride nanosheets associated with the exposure of multiple active sites, and synergistic effect between the CoN_y as OER active site and favorable charge transfer on CoO_x with abundance of oxygen vacancies.[32] In another report, Sun et al. showed that petal-like MoO_2@MoN core-shell nanosheets exhibited high HER and OER efficiency; this mainly contributed to the chemical coupling effect and strong electronic interaction between MoO_2 and MoN to enhance the electronic conductivity and charge transfer ability.[33] Nevertheless, despite the benefits mentioned, no binary metal nitride (Zn_3N_2-Co_2N) hybridized TMOs (Co_3O_4) material has yet been reported in the catalysis field for overall water splitting. Herein, we propose an advanced nanostructured material based on earth-abundant binary cobalt-zinc nitride nanorod arrays decorated with ultrafine Co_3O_4 nanoparticles supported on three-dimensional (3D) Ni foam (NF) (labeled as Co_3O_4 NPs/Co-Zn nitride), as an ideal electrocatalyst for HER/OER toward achieving remarkable performance of overall water splitting in alkaline conditions. Emphatically, the Co_3O_4 NPs/Co-Zn nitride catalyst enables a HER and OER current density of 10 mA cm^{-2} at very low overpotentials of 80.5 and 271.7 mV, respectively. Further, the findings demonstrate the rather small Tafel slope values of Co_3O_4 NPs/Co-Zn nitride catalyst for HER and OER of 54.4 and 52.4 mV dec^{-1}, respectively, which are solid evidence for the favorable HER and OER reaction kinetics under the help of our proposed catalyst. The result is that the electrolyzer with Co_3O_4 NPs/Co-Zn nitride as catalytic electrodes delivers current densities of 10 and 50 mA cm^{-2} at rather low cell voltages of 1.59 and 1.81 V, respectively, and is highly stable – at least, it can continuously operate for more than 60 h without damage to the catalytic performance.

Experimental

Chemical reagents

The $(CH_3COO)_2Co.4H_2O$, $Zn(NO_3)_2.6H_2O$, urea, NH_4F, HCl (37 %), NaOH, Nafion (5 wt %), KOH, acetone, Pt/C (20 wt % loading), ethanol, RuO_2 (99.9 %), and $Co(NO_3)_2.6H_2O$ were purchased from Sigma-Aldrich.

Synthesis of the Co_3O_4 NPs/Co-Zn nitride

The precursor cobalt-zinc carbonate hydroxide nanorod arrays supported on NF (labeled as Co-Zn-(OH-CO_3)) was prepared by a hydrothermal method (**see the Supporting Information (SI)** for the synthetic details). The as-prepared Co-Zn-(OH-CO_3) was then subjected to thermal nitridation under NH_3 atmosphere for 3 h at 500 °C with a heating rate of 2 °C min^{-1} to convert into nitride sample (labeled as Co-Zn nitride). The NH_3 flow rate applied was 50 sccm. Next, the obtained Co-Zn nitride was consecutively immersed in 1 mM mM $(CH_3COO)_2Co$ and 1 mM NaOH solutions for 30 min each, prior to calcination in Ar gas (100 sccm) for 2 h at 300 °C with a heating rate of 2 °C min^{-1}, to finally form Co_3O_4 NPs/Co-Zn nitride sample. The cobalt-zinc oxide nanorod arrays supported on NF (labeled as Co-Zn oxide) was also synthesized for comparison (**see the SI** for the synthetic details).

Material Characterization

Field-emission scanning electron microscopy (FE-SEM) images and energy dispersive X-ray spectroscopy (EDS) patterns of the products were conducted on Zeiss-Gemini 500. Transmission electron microscopy (TEM) measurements, high-resolution TEM (HR-TEM), and EDS mapping data were carried out on JEOL-JEM 2010. Powder X-ray diffraction (XRD) patterns of the products were collected by PANalytical-X'Pert PRO Multi-Purpose X-Ray Diffractometry with Cu-kα radiation (λ = 1.54 Å).

The X-ray photoelectron spectroscopy (XPS) spectra of all products were recorded in Thermo Fisher Scientific-Theta Probe. The Brunauer-Emmett-Teller (BET) specific surface area and pore size distribution of the products were acquired on Micromeritics Instrument-ASAP 2020 Plus system (USA). *In situ* Raman measurements were performed by A Raman spectrometer (Raman-touch, Nanophoton) with an excitation laser wavelength of 532 nm and a power of ca. 5 mW.

Electrochemical measurements

The electrochemical characterization of the products was conducted on CH660D workstation. Linear sweep voltammetry (LSV), cyclic voltammetry (CV), electrochemical impedance spectroscopy (EIS), and chronoamperometric measurements for HER and OER under alkaline conditions (1.0 M KOH electrolyte) were performed using a three-electrode test configuration, wherein the developed samples (1 cm × 1 cm), graphite rod, and Ag/AgCl were the working, counter, and reference electrodes, respectively. All LSV curves for HER and OER were compensated for ohmic resistance. In addition, all potentials were calibrated with respect to reversible hydrogen electrode (RHE). To evaluate the overall water splitting performance, the Co_3O_4 NPs/Co-Zn nitride was used as both catalytic cathode and catalytic anode to assemble an Co_3O_4 NPs/Co-Zn nitride (-, +) cell. The comparative cell based on Pt/C as a cathode catalyst and RuO_2 as an anode catalyst was also built for comparison (**see the SI** for the synthetic detail of the Pt/C- and RuO_2-based electrodes).

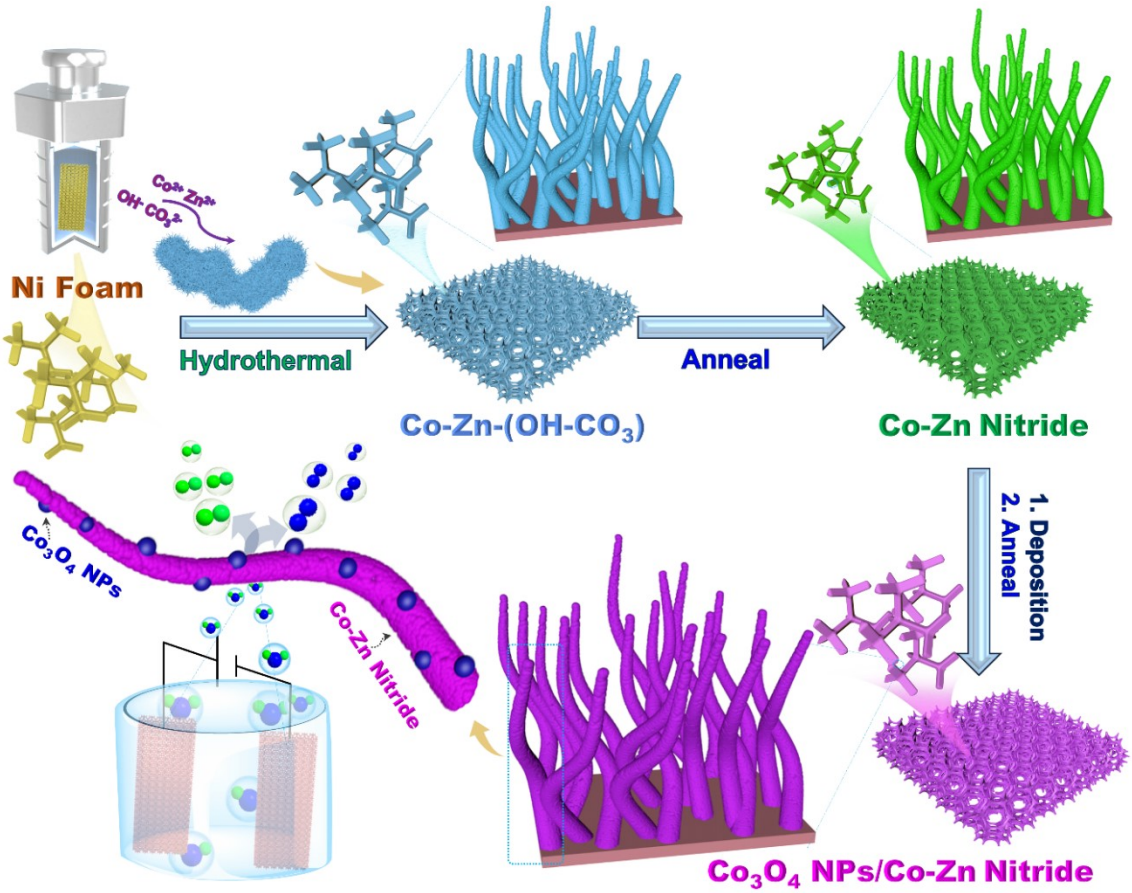

Scheme 1 A schematic of the synthetic procedure of the Co_3O_4 NPs/Co-Zn nitride

Results and discussion

Morphological and structural characterization

Scheme 1 depicts the synthetic protocol of the Co_3O_4 NPs/Co-Zn nitride. First, the Co-Zn-(OH-CO_3) nanorod arrays was deposited on the NF surface via a hydrothermal reaction, which is recognized as an effective method of nanomaterial fabrication owing to its facility and flexibility in morphology control. In this method, the reaction rate can be speeded up, accompanying by the occurrence of the unusual reaction, causing the formation of crystalline materials at rather low temperatures.[34] Fig. S1 reveals the quite smooth surface of the pre-treated NF, which contrasts with that of the Co-Zn-(OH-CO_3) sample (Fig. S2). The SEM images at low magnifications (Figs. S2a and b) reveal that the hydrothermal reaction gives the whole surface of the NF a coat of a secondary material. At high magnification (Figs. S2c and d), the secondary material presents arrays of solid nanorod features with average diameter of ~70 nm. The powder XRD analysis was then performed for Co-Zn-(OH-CO_3) sample to investigate its crystalline structure. As shown in Fig. S3, there are some obvious diffraction peaks observed from the XRD pattern of the Co-Zn-(OH-

CO_3), demonstrating its rather high crystallinity. The diffraction peaks centered at two theta of 28.4, 36.2, 39.1, 58.6, and 63.3° match well with the (021), (510), (-420), (-622), and (-821) planes of the $Zn_5(CO_3)_2(OH)_6$ (JCPDS No.19-1458),[35] and the other peaks centered at two theta of 33.8, 35.5, 36.5, 47.3, 59.9, and 62.2° should be assigned to the (221), (040), (231), (340), (412) and (450) planes of $Co_2CO_3(OH)_2$ (JCPDS No#48-0083) without any impurity.[36] Then, Co-Zn nitride was synthesized by the nitridation treatment of Co-Zn-(OH-CO_3) at high temperature in NH_3 atmosphere. Although the obtained Co-Zn nitride still retains the solid nanorod arrays feature of its parent (Figs. S4a and b), the surface of individual nanorods changes from smooth to relatively rough (Figs. S4c and d). Also, the nanorods tend toward connection with each other, which will provide effective pathways for electron transport along the whole proposed material, thereby significant improving the catalytic performance. After nitridation, the Co-Zn nitride sample is found to be comprised of two dominant phases, such as Zn_3N_2 (JCPDS No#035-0762),[37] corresponding to the diffraction peaks at two theta of 31.6, 34.2, 36.7, 43.3, and 70.7°, and Co_2N (JCPDS No#072-1368),[38] showing the diffraction peaks at two theta of 41.5, 42.6, 56.8, and 69.5° (Fig. S5). Finally, the Co_3O_4 NPs/Co-Zn nitride was acquired through the growth of Co_3O_4 nanoparticles (NPs) over the surface of Co-Zn nitride by precipitation method, combined with thermal treatment in air. The SEM images of Co_3O_4 NPs/Co-Zn nitride in Figs. 1a-c clearly show a large amount of uniform nanorod structure with apparent rough surface and uniform diameter of ~60 nm, which is very similar in the appearance of the Co-Zn nitride alone, suggesting that there is no influence on the pristine morphology, even under the harsh conditions of the growth process of the Co_3O_4 NPs. To explore the micromorphology of Co_3O_4 NPs/Co-Zn nitride, TEM measurement was also performed. Figs. 1d and e show the TEM images of the Co_3O_4 NPs/Co-Zn nitride at different magnifications. Clearly, the solid nanorod morphology with the rather rough surface feature of Co_3O_4 NPs/Co-Zn nitride is also confirmed by TEM observations. Such rough feature is anticipated to provide a larger number of catalytic active sites and endow the entire catalyst with a larger specific surface area than those of the smooth surface. The diameter of individual Co_3O_4 NPs/Co-Zn nitride nanorods is found to be about ~60 nm, which is consistent with the SEM result. Interestingly, the surface of the Co_3O_4 NPs/Co-Zn nitride nanorod is decorated with dark pots highlighted in white cycles, which can be assigned to the Co_3O_4 NPs, as displayed in the magnified TEM (Fig. 1e), HR-TEM, and EDS mapping images (Fig. S6). The content of Co_3O_4 NPs in the Co_3O_4 NPs/Co-Zn nitride sample was determined by XPS analysis, which exhibits that the Co percentage of Co_3O_4 NPs in the proposed sample is around 14.08 at % (Table S1).

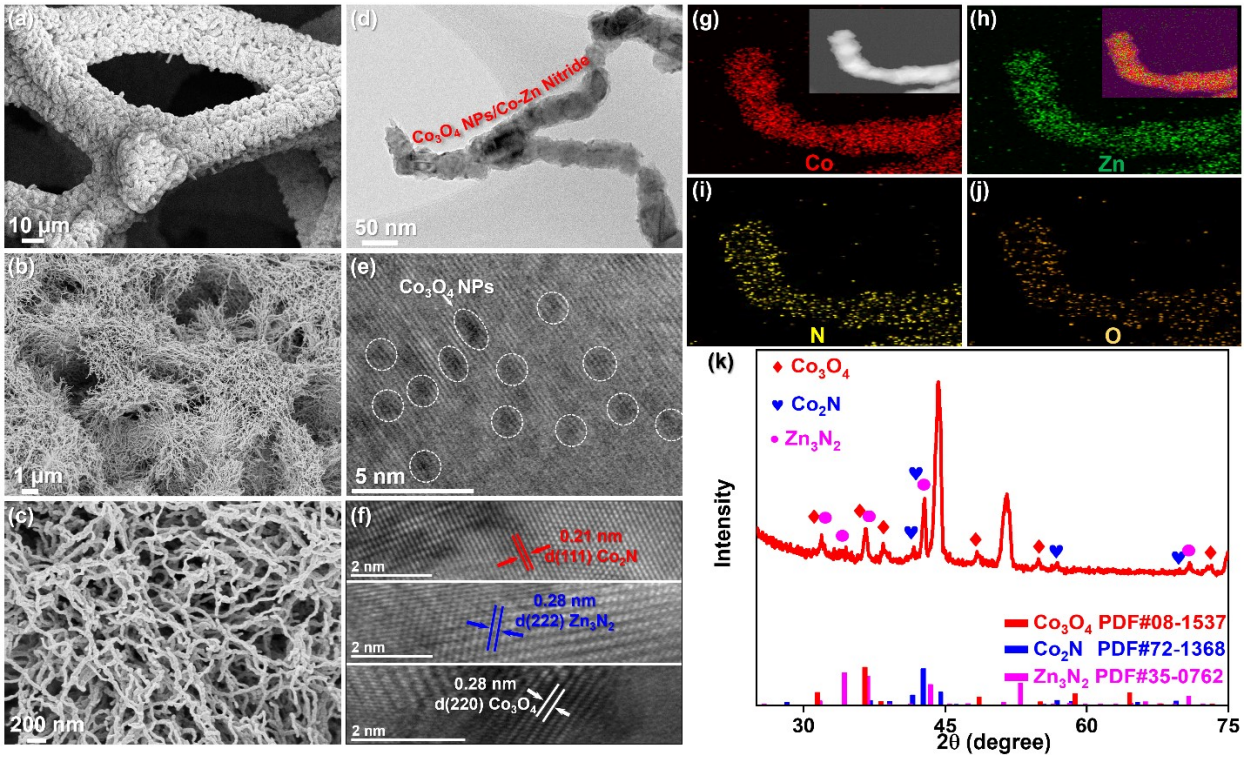

Fig. 1 (a)-(c) SEM images, (d) and (e) TEM images, (f) HR-TEM images, (g)-(j) EDS mapping images, and (k) XRD pattern of the Co_3O_4 NPs/Co-Zn nitride.

To determine the primary phases in the developed material, we also carried out high-resolution TEM (HR-TEM) analysis at the surface of individual Co_3O_4 NPs/Co-Zn nitride nanorods (Fig. 1f). Three different values are detected, including the lattice fringes of 0.21, 0.28, and 0.28 nm corresponding to the (111) plane of Co_2N, (222) plane of Zn_3N_2, and (220) plane of Co_3O_4, respectively, suggesting the existence of these three phases in the hybrid material. In addition to the Co_2N and Zn_3N_2 phases originating from the Co-Zn nitride template as mentioned above, the appearance of new phase proves that the dark pots over the surface of Co-Zn nitride is Co_3O_4. Indeed, according to the EDS mapping images represented in Figs. 1g-j, the individual Co_3O_4 NPs/Co-Zn nitride nanorod was confirmed to be a

compound of four elements, namely Zn, Co, N, and O. Further, the XRD pattern in Fig. 1k corroborates that the Co_3O_4 NPs/Co-Zn nitride contains three separated phases, such as Co_2N, Zn_3N_2, and Co_3O_4 (JCPDS No#080-1537),[39] which matches well with the diffraction peaks at two theta of 30.9, 36.4, 48.5, 55.0 and 76.5°. The transformation of chemical composition from the pure NF to the Co_3O_4 NPs/Co-Zn nitride was observed from EDS analysis; the EDS spectra of the pure NF, Co-Zn-(OH-CO_3), Co-Zn nitride alone, and Co_3O_4 NPs/Co-Zn nitride are represented in Fig. S7. Only the Ni element can be observed from the EDS spectrum of the NF (Fig. S7a), while after hydrothermal reaction, the signals of the Zn, Co, C, and O elements were detected from the Co-Zn-(OH-CO_3) (Fig. S7b), consistent with the $Zn_5(CO_3)_2(OH)_6$ and $Co_2CO_3(OH)_2$ phases detected by XRD. Regarding the Co-Zn nitride (Fig. S7c), in addition to the Zn and Co elements, the appearance of N element instead of C demonstrates the complete conversion into nitride phases (Zn_3N_2 and Co_2N) after the nitridation treatment. Finally, the EDS spectrum of the Co_3O_4 NPs/Co-Zn nitride shows the presence of Zn, Co, N, and O elements, which is in line with the XRD and EDS mapping results.

Next, we performed XPS analysis for the Co_3O_4 NPs/Co-Zn nitride to further investigate the chemical environment of the surface element. More importantly, the XPS is a useful measurement to confirm whether or not there has been charge redistribution within the heterostructure of the Co_3O_4 NPs/Co-Zn nitride. Fig. 2a shows the XPS survey spectra of the Co_3O_4 NPs/Co-Zn nitride and Co-Zn nitride, which reveals that all the required elements of Zn, Co, N, and O are detected. To evidence the electron interaction occurring in the Co_3O_4 NPs/Co-Zn nitride heterostructure, we compare the high-resolution XPS spectra of the Co_3O_4 NPs/Co-Zn nitride and Co-Zn nitride (Figs. 2b-e). The Zn 2p spectrum of the pristine Co-Zn nitride was fitted, and the result in Fig. 2b shows two peaks at binding energies of 1022 and 1045.2 eV that can be ascribed to the Zn $2p_{3/2}$ and Zn $2p_{1/2}$ characteristic peaks of the Zn_3N_2 phase, respectively.[40] After the introduction of the Co_3O_4 NPs, the binding energies of the Zn $2p_{3/2}$ and Zn $2p_{1/2}$ peaks in the Co_3O_4 NPs/Co-Zn nitride hybrid structure exhibit a slightly positive shift of around 0.3 eV, suggesting an increase in positive charges of Zn ion.[41] In the Co 2p XPS spectrum of the Co-Zn nitride (Fig. 2c), there are two dominant peaks centered at binding energies of 780.8 and 796.0 eV, which index to the Co $2p_{3/2}$ and Co $2p_{1/2}$ characteristic peaks of the Co_2N phase.[42] Additionally, two shake-up satellite peaks at higher binding energies indicate that the Co^{2+} is the main oxidation state of Co in this heterostructure.[43] Regarding the Co_3O_4 NPs/Co-Zn nitride, the Co 2p XPS spectrum is rather different from that of its counterpart. The new peaks at binding energies of 779.5 and 794.8 eV for Co $2p_{3/2}$ and Co $2p_{1/2}$, respectively, originate from the Co^{3+} of Co_3O_4 phase; in addition, those at binding energies of 781.2 and 795.9 eV for Co $2p_{3/2}$ and Co $2p_{1/2}$ belong to the Co^{2+} of Co_3O_4, demonstrating the formation of new phase Co_3O_4 in the hybrid material.[40] Like Zn 2p, the characteristic peaks of Co_2N show a slight shift to higher binding energies, evidencing the modulation of electronic structure of Co atoms after engineering by the guest Co_3O_4. As represented in Fig. 2d, the N 1s XPS spectrum of the Co-Zn nitride sample is deconvoluted into six peaks at 395.4, 396.1, 397.7, 399.6, 401.4, and 403.2 eV, which are due to the Zn-N bond, Co-N bond, pyridinic-N, pyrrolic-N, graphitic-N, and oxidized-N, respectively,[40,44,45] whereas the N 1s XPS peaks of the Co_3O_4 NPs/Co-Zn nitride are positively shifted, compared to the pristine sample. The shifts of the Zn 2p, Co 2p, and N 1s peaks of the Co_3O_4 NPs/Co-Zn nitride in the direction of higher binding energies than those of the pristine Co-Zn nitride demonstrate the presence of a strong electron interaction between the host Co-Zn nitride and the guest Co_3O_4. The deposition of Co_3O_4 over the surface of Co-Zn nitride causes charge redistribution between Co_3O_4 and Zn_3N_2/Co_2N, which can effectively regulate the electronic structure of both Co and Zn across the heterointerface, and thereby significantly improve their electrocatalytic activity.[46,47] For the O 1s XPS spectrum of the Co_3O_4 NPs/Co-Zn nitride in Fig. 2e, the peak at binding energy of 529.7 eV corresponds to the Co-O bond belonging to Co_3O_4 phase, while the peaks at binding energies of 531.5 and 532.6 eV are assigned to the hydroxyl group and weakly adsorbed water, respectively.[48,49] According to the XPS results, the incorporation of Co_3O_4 and Co-Zn nitride brings a strong electron interaction between them, and thus electronic structure of the atoms centered near the heterointerface region is tailored. Such charge redistribution can be anticipated to endow the entire Co_3O_4 NPs/Co-Zn nitride material with excellent catalytic activity for both HER and OER toward effective boosting of the overall water splitting.

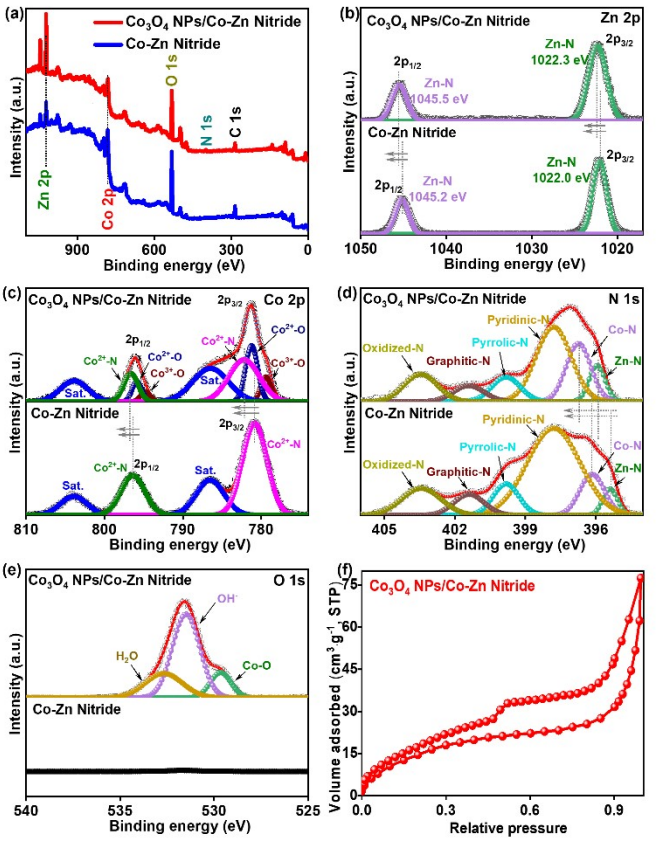

Fig. 2 (a) XPS survey spectra and (b)-(e) high-resolution XPS spectra of the Zn 2p, Co 2p, N 1s, and O 1s for the Co-Zn nitride and Co_3O_4 NPs/Co-Zn nitride. (f) N_2 adsorption-desorption isotherm of the Co_3O_4 NPs/Co-Zn nitride.

In addition to the optimal electronic structure, the Co_3O_4 NPs/Co-Zn nitride with multi-dimensional structure, including zero-dimensional structure of Co_3O_4 NPs, one-dimensional structure of Co-Zn nitride

nanorod arrays, and 3D structure of NF substrate, is expected to provide a large surface area with abundant exposure of catalytic active sites, which can effectively support the catalysis of electrochemical reactions on a geometric basis. The specific surface area is estimated using N_2 adsorption-desorption isothermal test on Co_3O_4 NPs/Co-Zn nitride. As exemplified in Fig. 2f, the Co_3O_4 NPs/Co-Zn nitride possesses a relative high BET specific surface area of 57.2 $m^2 g^{-1}$, which exceeds that of other earth-abundant transition metal-based electrocatalysts reported elsewhere ZnO/AuNP-30 with 10.5 $m^2 g^{-1}$, Co-FeOOH@Ir-Co(OH)F with 30 $m^2 g^{-1}$, and 1T-VS_2@N with 47 $m^2 g^{-1}$.[50–52] It is also worth noting that all features of the obtained isotherm match well with the typical IUPAC type IV pattern with the existence of hysteresis loop, suggesting the existence of mesopores with the hybrid structure. Indeed, the pore size distribution in Fig. S8 reveals the highest peaks at pore diameter range 1.2 to 10 nm, which belong to the meso-range. The Co_3O_4 NPs/Co-Zn nitride with large amount of mesopores can expose more active sites to contact more reactant molecules, and facilitate the charge/mass transfer at the contacting interfaces, which is more beneficial to the reaction kinetics of HER and OER in the process of electrochemical water splitting.[53]

Electrocatalytic performance

Electrochemical activity for HER

The proposed Co_3O_4 NPs/Co-Zn nitride sample is expected to effectively catalyze the HER, OER, and overall water splitting processes, owing to its twin advantages of physicochemical property and structure. We firstly assessed the electrocatalytic property of the Co_3O_4 NPs/Co-Zn nitride for alkaline HER using a standard three-electrode configuration. The control samples, such as Co-Zn nitride, Co-Zn oxide, and Co-Zn-(OH-CO_3), and commercial Pt/C catalyst, were also tested for comparison. As seen in Fig. 3a, the Co_3O_4 NPs/Co-Zn nitride shows a highly catalytic property for HER, with current densities of 10 and 50 mA cm^{-2} at low overpotentials of 80.5 and 121.7 mV, respectively. Notably, the Co_3O_4 NPs/Co-Zn nitride activity is negligibly poorer than that of the Pt/C with overpotential of 51.7 and 119.0 mV at the same current densities; however, it displays much better activity than those of the Co-Zn nitride, Co-Zn oxide, and Co-Zn-(OH-CO_3), supporting by the much higher overpotentials of these counterparts at the same current densities.

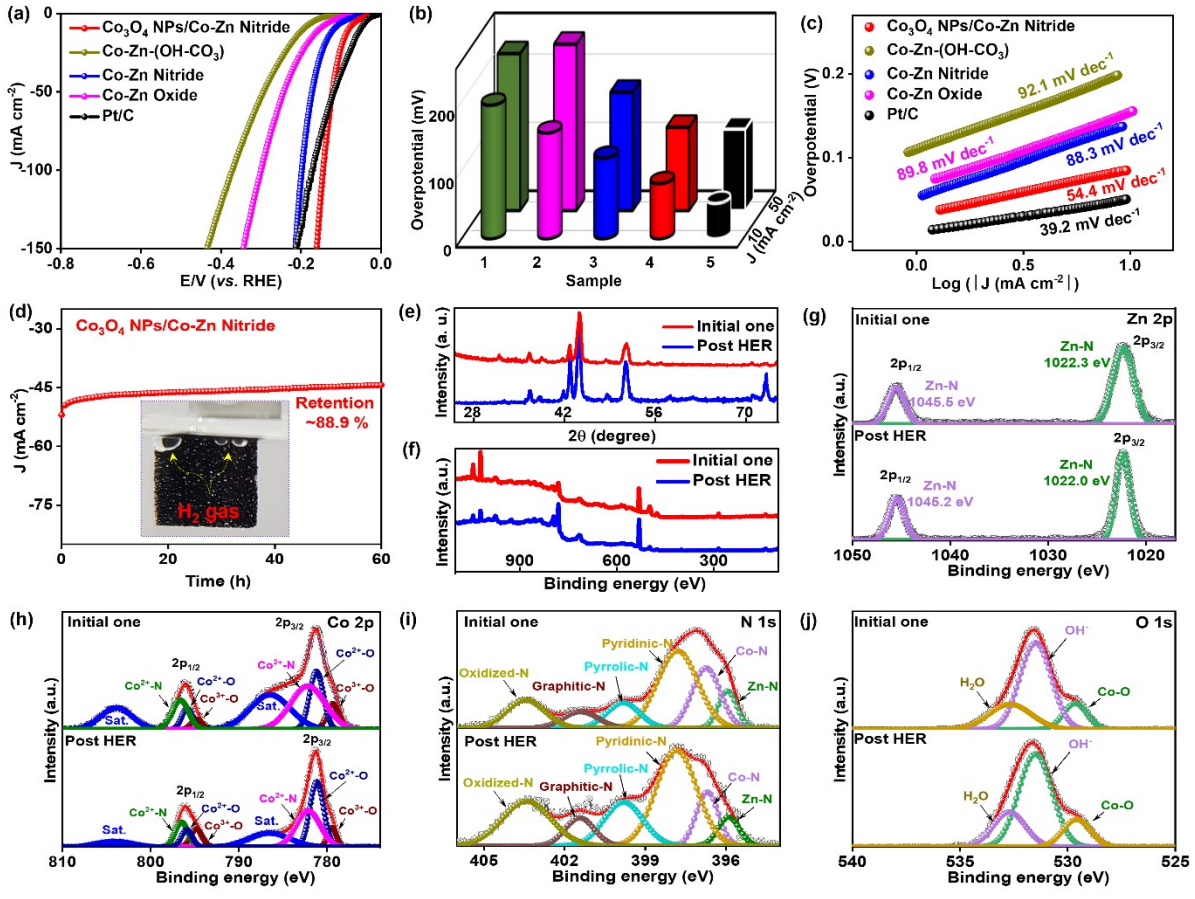

Fig. 3 HER performance: (a) LSV curves, (b) overpotentials at 10 and 50 mA cm^{-2} and (c) Tafel plots of the Co_3O_4 NPs/Co-Zn nitride (4) and its counterparts: Co-Zn nitride (3), Co-Zn oxide (2), and Co-Zn-(OH-CO_3) (1), and Pt/C commercial catalyst (5); (d) Chronoamperometric curve of the Co_3O_4 NPs/Co-Zn nitride at constant applied potential of 121.7 mV. (e) XRD patterns, (f) XPS survey spectra, and (g)-(j) high-resolution XPS spectra of the Zn 2p, Co 2p, N 1s, and O 1s for the post-HER Co_3O_4 NPs/Co-Zn nitride and the fresh sample.

The Co-Zn nitride, Co-Zn oxide, and Co-Zn-(OH-CO_3) afford current density of 10 mA cm^{-2} at overpotential of 117.8, 154.5, and 195.1 mV, respectively (Fig. 3b). Thus, the Co_3O_4 NPs/Co-Zn nitride catalyzes the alkaline HER the most effectively among its counterparts; furthermore, our material is also among the best noble-metal-free HER electrocatalysts, as listed in Table S2. Fig. 3c depicts the Tafel plots for the Co_3O_4 NPs/Co-Zn nitride, Co-Zn nitride, Co-Zn oxide, Co-Zn-(OH-CO_3), and Pt/C. As seen, the Pt/C commercial catalyst gives the smallest Tafel slope of 39.2 mV dec^{-1}. For the Co_3O_4 NPs/Co-Zn nitride, its Tafel slope value of 54.4 mV dec^{-1} is lower than those of the Co-Zn nitride, Co-Zn oxide, and Co-Zn-(OH-CO_3) of 88.3, 89.5, 92.1 mV dec^{-1}, respectively. Such smaller value indicates that the Co_3O_4 NPs/Co-Zn nitride can bring more favorable and faster reaction kinetics to the HER process, compared to the controlled samples. Furthermore, we also used the Tafel slope values to determine the predominant mechanism of the HER under the action of the Co_3O_4 NPs/Co-Zn nitride. The measured Tafel slope of 54.4 mV dec^{-1} suggests that the HER taking place on the active surface of the Co_3O_4 NPs/Co-Zn nitride follows the Volmer-Heyrovsky mechanism, as described by the following equations:[54]

$$H_2O + e^- \rightarrow H_{ads} + OH^- \quad \text{(Volmer reaction)} \quad (1)$$

$$H_{ads} + H_2O + e^- \rightarrow H_2 + OH^- \quad \text{(Heyrovsky reaction)} \quad (2)$$

Next, we carried out multi-step chronopotentiometric measurement for the Co_3O_4 NPs/Co-Zn nitride under HER to probe its stability. Under HER conditions (Fig. S9), when the applied potential increases from 80.5 to 143.4 mV, the response current density also increases from 10 to 100 mA cm^{-2}; interestingly, these response current densities seem to switch rather quickly, and maintain their stable state for at least 500 s at each potential, suggesting remarkable stability, high catalytic activity, and excellent mass transport character. Interestingly, such excellent mass transport nature accelerates the diffusion of reactant, electrolyte, and products along its structure, which is beneficial to the HER performance, even in the harsh conditions of continuously changing applied potentials.[54] The durability of the Co_3O_4 NPs/Co-Zn nitride was further evaluated under alkaline HER conditions by recording the chronoamperometric curve at constant potential for 60 h. Fig. 3d reveals that the electrocatalytic activity of the Co_3O_4 NPs/Co-Zn nitride is retained well, with current density retention of 98.9 %, after 60 h. The high stability of the Co_3O_4 NPs/Co-Zn nitride supports the stable release of H_2 and O_2 bubbles over its surface for long reaction time, as seen in the inset of Fig. 3d. The stable catalytic activity of the Co_3O_4 NPs/Co-Zn nitride is further proven by the overlap of the fresh LSV curve and that recorded after long-term testing (Fig. S10a). Even after 60 h operation, the overpotentials of the post-HER Co_3O_4 NPs/Co-Zn nitride at current densities of 10 and 50 mA cm^{-2} are negligibly higher than those of the fresh one (Fig. S10b). Also, the SEM, TEM, and EDS elemental mapping images in Fig. S11 evidence the remaining morphology and microstructure, as well as the unchanged chemical composition, of the post-HER Co_3O_4 NPs/Co-Zn nitride. We then performed XRD measurement to determine the phase of post-HER sample. As shown in Fig. 3e, all diffraction peaks observed from the XRD pattern of the post-HER Co_3O_4 NPs/Co-Zn nitride are in line with the phases of Co_2N, Zn_3N_2, and Co_3O_4, reconfirming the chemical stability of our proposed material. XPS measurement was also employed to identify the valance state of the Co_3O_4 NPs/Co-Zn nitride after long-term catalysis of the HER. The obtained XPS survey spectrum in Fig. 3f reveals that the Zn, Co, N, and O elements are the primary components in the post-HER sample. By fitting the Zn 2p, Co 2p, N 1s, and O 1s XPS spectra of the post-HER Co_3O_4 NPs/Co-Zn nitride (Figs. 3g-j), all obtained peaks index well to the Co-N bond in Co_2N phase, Zn^{2+} oxidation state in Zn_3N_2 phase, and Co^{2+} and Co^{3+} oxidation states of Co_3O_4 phase, highly consistent with the XPS result of the fresh sample. Therefore, all experimental results mentioned above demonstrate that the Co_3O_4 NPs/Co-Zn nitride serves as a highly active and stable electrocatalyst for the HER in alkaline conditions.

Electrochemical activity for the OER

In addition to the excellent catalytic activity of the Co_3O_4 NPs/Co-Zn nitride for alkaline HER, it is anticipated that the Co_3O_4 NPs/Co-Zn nitride can effectively catalyze the anodic electrochemical reaction: OER of the water splitting owing to its unique advantages of geometric and electronic structure. The catalytic performance of the Co_3O_4 NPs/Co-Zn nitride was thus examined for OER in 1.0 M KOH electrolyte. Also, the OER catalytic performance of its counterparts and the commercial RuO_2 was probed for comparison. From the LSV curves in Fig. 4a, the overpotentials at current densities of 10 and 50 mA cm^{-2} are determined for all these products, and Fig. 4b presents the results. The Co_3O_4 NPs/Co-Zn nitride can deliver 10 and 50 mA cm^{-2} at overpotentials of 271.7 and 335.8 mV, respectively, which are much lower values than those of the Co-Zn nitride with overpotentials of 284.6 and 363.5 mV, Co-Zn oxide with overpotentials of 293.4 and 368.5 mV, or Co-Zn-(OH-CO_3) with overpotentials of 337.8 and 396.6 mV at the same current densities. Obviously, the successful conversion into nitride state and the integration of Co_3O_4 NPs resulting in charge redistribution account for the better OER performance of the Co_3O_4 NPs/Co-Zn nitride than those of the control samples. Importantly, the Co_3O_4 NPs/Co-Zn nitride outperforms the RuO_2 commercial catalyst; the overpotentials of RuO_2 are 335.4 and 438.9 mV at current densities of 10 and 50 mA cm^{-2}, respectively (Fig. 4b). Furthermore, the Co_3O_4 NPs/Co-Zn nitride shows the higher catalytic activity for OER than OER electrocatalysts based on the non-noble metals reported elsewhere, as listed in Table S3. Then, we calculated the Tafel slope of the products and RuO_2 catalyst according to the LSV results to elucidate the OER reaction kinetics (Fig. 4c). The Tafel slope of 52.4 mV dec^{-1} is obtained for the Co_3O_4 NPs/Co-Zn nitride, which is lower than those of the Co-Zn nitride, Co-Zn oxide, Co-Zn-(OH-CO_3), and RuO_2 with 87.3, 87.6, 87.8, and 111.8 mV dec^{-1}, respectively. Such small Tafel slope value indicates the most favorable kinetics of the OER under the help of the Co_3O_4 NPs/Co-Zn nitride, which allow the oxygen evolution on the Co_3O_4 NPs/Co-Zn nitride surface to occur at the lowest overpotential, compared to those on the comparative samples, even on the commercial RuO_2 catalyst. To evaluate the stability and durability of the Co_3O_4 NPs/Co-Zn nitride under OER conditions, multi-step chronopotentiometric measurement was performed (Fig. S12). As under the HER conditions, the current densities instantly respond to the changed the applied potentials (from 1.50 to 1.60 V), and the corresponding current densities are stable for at least 500 s at each step. This phenomenon demonstrates

that the Co_3O_4 NPs/Co-Zn nitride possesses by nature an extraordinary mass transport for OER process, which leads to the high OER performance, and good OER stability. Next, its stability for OER was deeply investigated by chronoamperometric measurement at constant voltage of 335.8 V for 60 h. Fig. 4d shows the stable state of the resultant current density throughout the stability testing; the Co_3O_4 NPs/Co-Zn nitride exhibits a very high current density retention of 87.6 % after long-term operation. The Inset of Fig. 4d presents the surface of Co_3O_4 NPs/Co-Zn nitride catalytic electrode during the chronoamperometric testing; it clearly reveals the formation of a large amount of O_2 bubbles over the electrode surface, reconfirming the superior OER activity of our proposed material. Further, the LSV curve recorded after stability testing shows a subtle difference, compared to the fresh one (Fig. S13a). The comparison of overpotentials at current densities of 10 and 50 mA cm^{-2} obtained before and after stability testing also shows a subtle difference (Fig. S13b). The SEM and TEM images of the post-OER Co_3O_4 NPs/Co-Zn nitride in Figs. S14a-c show a negligible aggregation of nanorods; however, the morphology feature of nanorod is still similar to the fresh sample. Turning to the chemical composition, the EDS elemental mapping images (Figs. S14d-g) demonstrate that all the required elements, such as Zn, Co, N, and O, appear in the post-OER Co_3O_4 NPs/Co-Zn nitride. Notably, the density of O element becomes higher, compared to the fresh Co_3O_4 NPs/Co-Zn nitride, suggesting that the nitride phase may be partially oxidized on their surface, resulting in the formation of *in situ* oxidation phases, which is regarded as real active sites for OER. The magnified TEM images of the post-OER sample in Figs. S15a and b reveal that there is a thin layer covering the Co_3O_4 NPs/Co-Zn nitride surface after long-term catalysis of the OER. Corresponding HR-TEM images of the shell layer in Figs. S15c and d exhibit the estimated lattice fringe of 0.198 nm matching with the (104) plane of CoOOH, respectively. The findings further suggest that the CoOOH phase is formed over the catalyst surface after stability testing under the OER conditions.

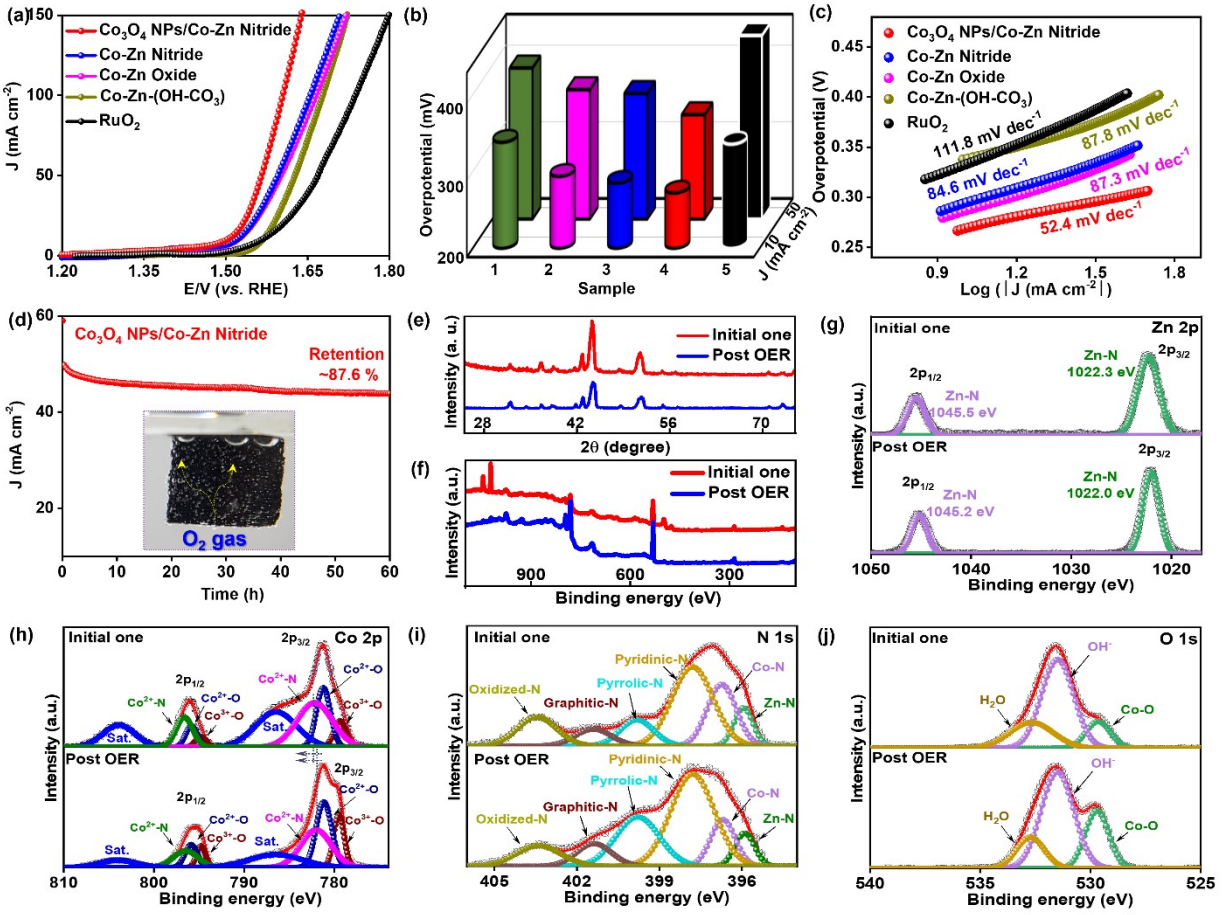

Fig. 4 OER performance: (a) LSV curves, (b) overpotentials at 10 and 50 mA cm^{-2} and (c) Tafel plots of the Co_3O_4 NPs/Co-Zn nitride (4) and its counterparts: Co-Zn nitride (3), Co-Zn oxide (2), and Co-Zn-($OH-CO_3$) (1), and RuO_2 commercial catalyst (5); (d) Chronoamperometric curve of the Co_3O_4 NPs/Co-Zn nitride at constant applied potential of 1.56 V. (e) XRD patterns, (f) XPS survey spectra, and (g)-(j) high-resolution XPS spectra of the Zn 2p, Co 2p, N 1s, and O 1s for the post-OER Co_3O_4 NPs/Co-Zn nitride, and the fresh sample.

XRD and XPS measurements were then performed for the post-OER Co_3O_4 NPs/Co-Zn nitride to gain insight into its changes after the stability testing. All characteristic peaks of the Co_3O_4, Co_2N, and Zn_3N_2 phases are observed from the XRD pattern of the post-OER sample, as shown in Fig. 4e. Furthermore, the XRD pattern of the post-OER Co_3O_4 NPs/Co-Zn nitride does not significantly change in

comparison with the fresh sample, reconfirming the high structural stability of the Co_3O_4 NPs/Co-Zn nitride during long-term operation. The XPS survey spectrum of the post-OER Co_3O_4 NPs/Co-Zn nitride (Fig. 4f) reveals the typical peaks for Zn 2p, Co 2p, N 1s, and O1s, which is similar in appearance to the fresh sample. In the Zn 2p XPS spectrum of the post-OER Co_3O_4 NPs/Co-Zn nitride (Fig. 4g), the Zn $2p_{3/2}$ and Zn $2p_{1/2}$ typical peaks of the Zn_3N_2 phase can be observed even after the stability testing, which are unchanged in comparison with that Zn 2p of the fresh sample, confirming the good chemical surface of the Zn_3N_2. In contrast, in the Co 2p XPS spectrum of the post-OER Co_3O_4 NPs/Co-Zn nitride (Fig. 4h), the Co $2p_{3/2}$ peak belonging to Co_2N phase has a slight shift in the direction of lower binding energy than that of the fresh sample, suggesting the partial transformation of Co^{2+} for Co_2N phase into higher oxidation state, such as Co^{3+} for the cobalt oxide/hydroxide phases.[55,56] Indeed, the increase in intensity of Co^{3+} peak in the Co 2p of the post-OER sample compared to the fresh one, is further supported by the supposition mentioned above. Also, Fig. 4i displays the decrease in intensities of the typical peak of Co-N bond in the N 1s XPS spectrum after the stability testing, while Fig. 4j shows the enhancement of peak intensity belonging to the O ion in the crystal lattice in the O 1s XPS spectrum of the post-OER sample. These observations are additive evidence for the *in situ* formation of oxidation phases over the Co_3O_4 NPs/Co-Zn nitride catalyst after long-term water oxidation.

Characterization of phase reconstruction during the HER and OER processes

In situ Raman measurements were conducted at various applied potentials to investigate the dynamic phase reconstruction of Co_3O_4 NPs/Co-Zn nitride under the HER and OER conditions toward deeply understanding the long-term dynamic structure-performance correlation. The *in situ* Raman data of the Co_3O_4 NPs/Co-Zn nitride sample under HER conditions is showed in Fig. 5a. As seen, three types of vibration peaks corresponding to the three compounds are observed from the Raman spectra of the Co_3O_4 NPs/Co-Zn nitride. The peaks at 265 cm^{-1} are concerned with the Raman-active photo modes in the Zn_3N_2 phase,[57] while the peaks at 473, 513, and 667 cm^{-1} are in line with the cobalt nitride phase.[58] In addition, the other smaller peaks at 482 and 512 cm^{-1} can be attributed to the E_g, F_{2g}, and A_{1g} vibration modes of Co_3O_4, respectively.[59] Thus, the *in situ* Raman results reconfirm the coexistence of Zn_3N_2, Co_2N, and Co_3O_4 phases in the Co_3O_4 NPs/Co-Zn nitride sample. Moreover, *in situ* Raman spectra under the HER conditions show the slight difference in intensity and shape of peaks between applied potential of 0 V and the others. This can be attributed to the formation of gas bubbles, which cover the surface of Co_3O_4 NPs/Co-Zn nitride sample, during the analysis of *in situ* Raman at different applied potentials, except for 0 V (Fig. S16).[60,61] More importantly, the Raman spectra shows that the characteristic peaks of Zn_3N_2, Co_2N, and Co_3O_4 phases are unchanged during catalysis of the HER process at applied potentials from -0.080 to -0.132 V, suggesting that there is no phase reconstruction occurring on the surface of the Co_3O_4 NPs/Co-Zn nitride heterostructure under the HER circumstance event at high applied voltages; in other words, the *in situ* Raman analysis corroborates the excellent structural endurability of our proposed materials under HER, which is consistent with the XRD and XPS results of the post-HER Co_3O_4 NPs/Co-Zn nitride.

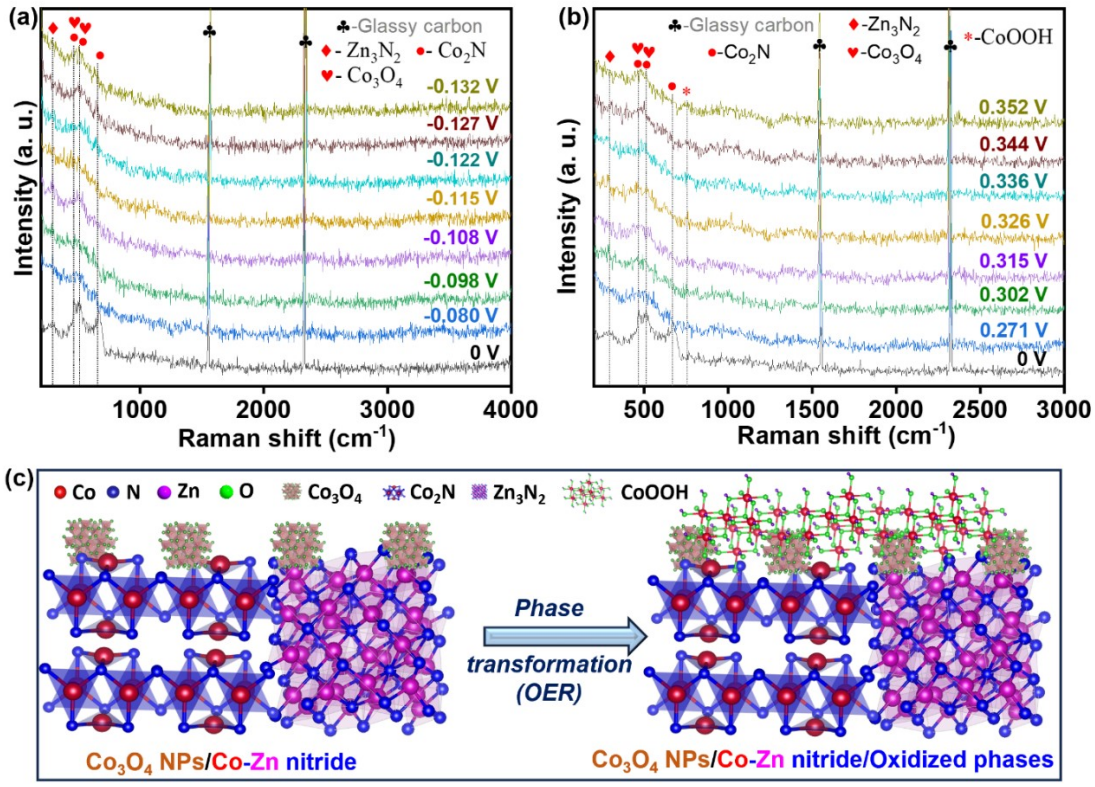

Fig. 5 *In situ* Raman spectra of the Co_3O_4 NPs/Co-Zn nitride under (a) HER conditions, and (b) OER conditions. (c) A schematic of the phase transformation of the Co_3O_4 NPs/Co-Zn nitride surface during catalysis of the OER process.

The slight change in intensity of the peaks (< 600 cm^{-1}) at applied potentials of -0.098 V and -0.115 V is assigned to the difference in density of gas bubbles covering the sample surface at different applied potentials. Regarding the OER conditions (Fig. 5b), all typical vibration peaks of the main phases such as Zn_3N_2, Co_2N, and Co_3O_4 are detected by in situ Raman analysis of Co_3O_4 NPs/Co-Zn nitride. Like the HER, the difference in intensity and shape of the detected peaks between applied potential of 0 V and the others is observed from in-situ Raman spectra of Co_3O_4 NPs/Co-Zn nitride under OER conditions. This may be due to the influence of evolved gas bubbles. Interestingly, Figure 5b also reveals that when the applied voltage exceeds 0 V, an additive Raman peak at 750.9 cm^{-1}, which is ascribed to the CoOOH phase, is detected in addition to the typical vibration peaks of the Zn_3N_2, Co_2N, and Co_3O_4.[62] The vibration peak belonging to the CoOOH phase tend to enhance in terms of its intensity on increasing the applied voltages. At the same time, the intensity of peak belonging to Co_2N phase at 667 cm^{-1} tends to reduce when increasing the applied voltage and this peak almost disappears at applied potential of 0.302 V. This suggest that during OER, the cobalt nitride phase gradually converts to CoOOH, which is a really active site for the OER process. The findings are solid evidence for the surface oxidation of Co_3O_4 NPs/Co-Zn nitride during the OER catalysis, consistent with the XRD and XPS results of the post-OER Co_3O_4 NPs/Co-Zn nitride. Therefore, *in situ* Raman analyses clarify the phase reconstruction of the Co_3O_4 NPs/Co-Zn nitride during the OER. It can be imagined that the cobalt nitride phase on the surface of the proposed heterostructure is partially oxidized to form oxide/hydroxide phases over the catalyst surface, as illustrated in Fig. 5c. These findings are in line with most research results regarding Co-based electrocatalysts for OER.[63] These additive electrocatalytic centers will contribute to the excellent performance of the Co_3O_4 NPs/Co-Zn nitride for OER process toward further enhanced water-splitting performance, in addition to its twin merits of optimized electronic structure, and unique morphology.

Electrochemical activity for overall water splitting

Given its promising electrocatalytic performance and high stability for both the HER and OER, the Co_3O_4 NPs/Co-Zn nitride is employed as both cathode and anode in a lab-made electrolyzer device (Fig. 6a), and we performed a series of experimental tests to evaluate its overall water splitting performance. The LSV curves in Fig. 6b show that the electrolyzer using Co_3O_4 NPs/Co-Zn nitride electrode has exceptional electrocatalytic performance, which is rather analogous to the electrolyzer using the Pt/C and RuO_2 commercial electrodes. Our Co_3O_4 NPs/Co-Zn nitride-based electrolyzer can afford water-splitting current densities of 10 and 50 mA cm^{-2} at cell voltages of 1.59 and 1.81 V, respectively. Meanwhile, the electrolyzer based on Pt/C and RuO_2 can deliver water-splitting current densities of 10 and 50 mA cm^{-2} at cell voltages of 1.62 and 1.84 V, respectively, which are slightly higher than those of our device (Fig. 6c). The comparison of cell voltage at 10 mA cm^{-2} between our device and the other devices based on non-noble metal bifunctional electrocatalysts in the literature supports the better water-splitting performance of the Co_3O_4 NPs/Co-Zn nitride (Fig. 6d), thus demonstrating its better potential for large-scale applications. Moreover, the stability of these electrolyzers was investigated through recording their chronoamperometric curves (Fig. 6e). These show that the Co_3O_4 NPs/Co-Zn nitride-based electrolyzer is highly stable under overall water splitting conditions; it can run stably for at least 60 h with a current density retention of 88.3 %. In contrast, the comparative electrolyzer using Pt/C and RuO_2 can operate stably for merely 30 h, then its activity degrades rapidly, resulting in a low current density retention of 72.1 % after 60 h operation. The LSV recorded after stability testing of the Co_3O_4 NPs/Co-Zn nitride-based electrolyzer is quite the same as the initial one, along with a little change in cell voltages after long-term running (Figs. 6f, and Fig. S17). These results further support the good maintenance of the catalytic performance of the Co_3O_4 NPs/Co-Zn nitride, even after continuously catalyzing both the HER and OER under overall water splitting conditions. Fig. 6g shows that when using the Co_3O_4 NPs/Co-Zn nitride as both cathode and anode in the electrolyzer, the hydrogen and oxygen produced over its surface have a ratio of approximately 2:1. In addition, the amount of the produced hydrogen and oxygen is rather analogous to the theoretical values, suggesting that the Co_3O_4 NPs/Co-Zn nitride can afford a very high Faradaic efficiency (FE) for the HER and OER. Indeed, the FE values of 98.9 and 99.1 % are reached for hydrogen and oxygen production, respectively, emphasizing the high-efficiency electrochemical reactions for HER and OER under the action of the Co_3O_4 NPs/Co-Zn nitride catalyst. Therefore, small operating cell voltages, great potential for long-term operation without much degradation of electrocatalytic activity, and high FE values for hydrogen and oxygen productions are observed for the electrolyzer based on the Co_3O_4 NPs/Co-Zn nitride electrode, corroborating the great capability of our proposed material to meet the targeted replacement of noble metal electrocatalysts.

Subsequently, to further examine the charge-transfer property of the Co_3O_4 NPs/Co-Zn nitride under overall water splitting conditions, its EIS plot was recorded, along with the EIS plots of its counterparts for comparison. It can be clearly seen in Fig. 6h that the EIS semicircle diameter of the Co_3O_4 NPs/Co-Zn nitride is much smaller than those of the Co-Zn nitride, Co-Zn oxide, and Co-Zn-(OH-CO_3), suggesting that compared to the others, the Co_3O_4 NPs/Co-Zn nitride possesses a much smaller charge-transfer resistance (R_{ct}). Through fitting the EIS data by an equivalent circuit model (inset of Fig. 6h), the R_{ct} values are estimated to be 0.32, 0.81, 1.03, and 1.06 Ω for the Co_3O_4 NPs/Co-Zn nitride, Co-Zn nitride, Co-Zn oxide, and Co-Zn-(OH-CO_3), respectively. Thus, the electrochemical reactions under the action of the Co_3O_4 NPs/Co-Zn nitride will be faster kinetics than those of its counterparts, which can be attributed to the

better electron mobility of nitride phase than that of oxide/hydroxide phases, as well as the synergy of the Co_3O_4 NPs and Co-Zn nitride. In other words, the Co_3O_4 NPs/Co-Zn nitride has greatly enhanced the charge transferability, and thus shows excellent performance toward overall water splitting.

Thereafter, the electrochemically active surface area (ECSA) was determined by electrochemical double-layer capacitance (C_{dl}) measurement to assess the number of catalytically active sites on the surface of the developed catalysts. To calculate the C_{dl} value, CV analysis was performed at various scan rates in the non-Faradaic potential region, as seen in Fig. S18. The result in Fig. 6i displays that the Co_3O_4 NPs/Co-Zn nitride can give a C_{dl} value of 46.0 mF cm^{-2}, which is around 1.4, 3.8, and 7.4 times more remarkable than those of the Co-Zn nitride, Co-Zn oxide, and Co-Zn-(OH-CO_3), respectively. The ECSA value being in direct proportion to the C_{dl} value implies that the ECSA of the Co_3O_4 NPs/Co-Zn nitride is highest among the others. The tendency for decrease in the C_{dl} values corresponds well to the difference in the electrochemical activity of these materials, highlighting that the higher the ECSA, the more superior the electrochemical activity that can be achieved. These results prove that the greater abundance of catalytic active sites constitutes one of the most important reasons for the higher electrocatalytic activity of the Co_3O_4 NPs/Co-Zn nitride than those of its comparative samples.

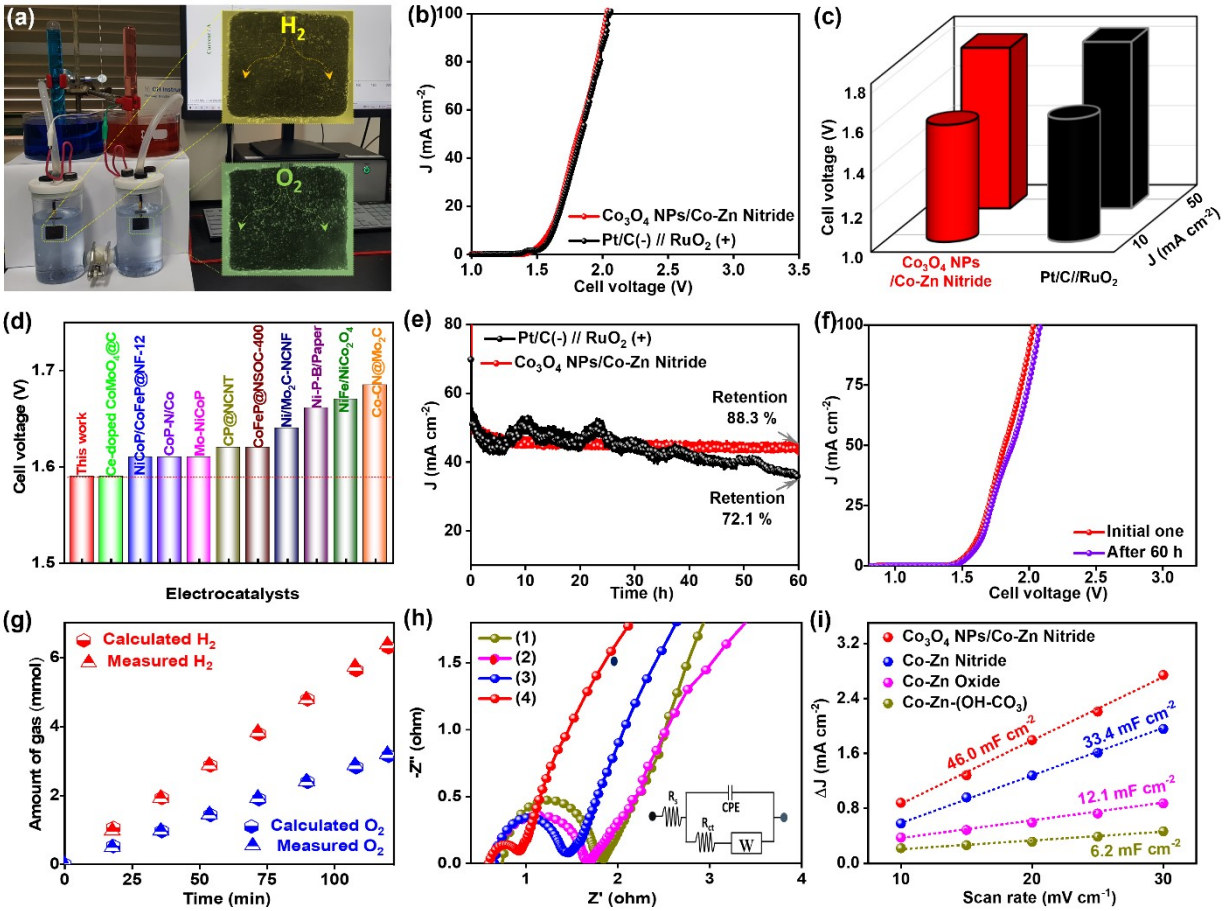

Fig. 6 (a) Photograph of the lab-made electrolyzer device using the Co_3O_4 NPs/Co-Zn nitride as both cathode and anode. (b) LSV curves of electrolyzer based on the Co_3O_4 NPs/Co-Zn nitride, and commercial Pt/C // RuO_2 catalysts. (c) Cell voltages of the electrolyzer based on the Co_3O_4 NPs/Co-Zn nitride at current densities of 10 and 50 mA cm^{-2}, compared to the electrolyzer based on Pt/C and RuO_2. (d) Cell voltages of the electrolyzer based on the Co_3O_4 NPs/Co-Zn nitride at current density of 10 mA cm^{-2}, compared to the other devices in the literature. (e) Chronoamperometric curve of the electrolyzer based on the Co_3O_4 NPs/Co-Zn nitride. (f) Cell voltages of the electrolyzer based on the Co_3O_4 NPs/Co-Zn nitride at current densities of 10 and 50 mA cm^{-2} after stability testing. (g) The amount of gas theoretically calculated and experimentally measured *vs.* time for HER and OER of the Co_3O_4 NPs/Co-Zn nitride electrode. (h) Nyquist plots of the Co_3O_4 NPs/Co-Zn nitride compared to its counterparts (the inset of (h) is an equivalent circuit model). (i) Current densities as a function of the scan rates of the Co_3O_4 NPs/Co-Zn nitride, Co-Zn nitride, Co-Zn oxide, and Co-Zn-(OH-CO_3) with the corresponding C_{dl} values, which are equal to the square roots of the corresponding slope values.

Conclusion

In summary, we successfully developed a novel nanostructured material based on binary metal nitride (Zn_3N_2-Co_2N) integrated with ultrathin Co_3O_4 nanoparticles. In addition to the advantages of morphological structure, the introduction of the guest Co_3O_4 endows the Co_3O_4 NPs/Co-Zn nitride material with a strong charge redistribution at the interfacial region, leading to further improve catalytic activity for both HER and OER toward overall water splitting. Thus, the Co_3O_4 NPs/Co-Zn nitride shows good catalytic behavior with very low overpotential of 80.5 and 217.7 mV at current density of 10 mA cm^{-2} for HER and OER, respectively. Remarkably, under overall water splitting conditions, the Co_3O_4 NPs/Co-Zn nitride electrode requires a small cell voltage of 1.59 and 1.81 V to gain 10 and 50 mA cm^{-2}, which approach that of the commercial Pt/C and RuO_2 catalysts, and surpasses those of the other bifunctional water splitting catalysts reported elsewhere. In addition, the Co_3O_4 NPs/Co-Zn nitride-based electrolyzer demonstrates a superior stability for water splitting, supported by the rather high current retention of 72.1 % after long-term electrolysis.

Acknowledgements

This research was supported by the Basic Science Research Program (2019R1A2C1004983) and the Regional Leading Research Center Program (2019R1A5A8080326) through the National Research Foundation funded by the Ministry of Science and ICT of Republic of Korea.

Notes and references

1 X. Han, X. Wu, Y. Deng, J. Liu, J. Lu, C. Zhong and W. Hu, *Adv. Energy Mater.*, 2018, **8**, 1800935.
2 T. L. L. Doan, D. C. Nguyen, P. M. Bacirhonde, A. S. Yasin, A. I. Rezk, N. Y. Dzade, C. S. Kim and C. H. Park, *Energy Environ. Mater.* 2023, **6**, e12407.
3 T. L. L. Doan, D. C. Nguyen, S. Prabhakaran, D. H. Kim, D. T. Tran, N. H. Kim and J. H. Lee, *Adv. Funct. Mater.*, 2021, **31**, 2100233.
4 J. Wang, J. Zhang, Y. Hu, H. Jiang and C. Li, *Sci. Bull.*, 2022, **67**, 1890–1897.
5 D. C. Nguyen, T. L. L. Doan, S. Prabhakaran, D. H. Kim, N. H. Kim and J. H. Lee, *Appl. Catal. B Environ.*, 2022, **313**, 121430.
6 C. Huang, D. Wu, P. Qin, K. Ding, C. Pi, Q. Ruan, H. Song, B. Gao, H. Chen and P. K. Chu, *Nano Energy*, 2020, **73**, 104788.
7 J. Zhang, Q. Xu, J. Wang, Y. Hu, H. Jiang and C. Li, *Sci. China Mater.*, 2023, **66**, 634–640.
8 D. C. Nguyen, D. T. Tran, T. L. Luyen Doan, N. H. Kim and J. H. Lee, *Chem. Mater.*, 2019, **31**, 2892–2904.
9 X. Zhu, D. C. Nguyen, S. Prabhakaran, D. H. Kim, N. H. Kim and J. H. Lee, *Mater. Today Nano*, 2023, **21**, 100296.
10 Q. Xu, J. Zhang, H. Zhang, L. Zhang, L. Chen, Y. Hu, H. Jiang and C. Li, *Energy Environ. Sci.*, 2021, **14**, 5228–5259.
11 J. Zhang, Q. Zhang and X. Feng, *Adv. Mater.*, 2019, **31**, 1808167.
12 C. Hu, L. Zhang and J. Gong, *Energy Environ. Sci.*, 2019, **12**, 2620–2645.
13 D. C. Nguyen, T. L. Luyen Doan, S. Prabhakaran, D. T. Tran, D. H. Kim, J. H. Lee and N. H. Kim, *Nano Energy*, 2021, **82**, 105750.
14 T. L. Luyen Doan, D. T. Tran, D. C. Nguyen, H. Tuan Le, N. H. Kim and J. H. Lee, *Appl. Catal. B Environ.*, 2020, **261**, 118268.
15 H. Over, *ACS Catal.*, 2021, **11**, 8848–8871.
16 D. C. Nguyen, D. T. Tran, T. L. L. Doan, D. H. Kim, N. H. Kim and J. H. Lee, *Adv. Energy Mater.*, 2020, **10**, 1903289.
17 S. Singh, D. C. Nguyen, N. H. Kim and J. H. Lee, *Chem. Eng. J.*, 2022, **442**, 136120.
18 X. Peng, C. Pi, X. Zhang, S. Li, K. Huo and P. K. Chu, *Sustain. Energy Fuels*, 2019, **3**, 366–381.
19 J. K. Nørskov, T. Bligaard, A. Logadottir, J. R. Kitchin, J. G. Chen, S. Pandelov and U. Stimming, *J. Electrochem. Soc.*, 2005, **152**, J23.
20 W.-F. Chen, K. Sasaki, C. Ma, A. I. Frenkel, N. Marinkovic, J. T. Muckerman, Y. Zhu and R. R. Adzic, *Angew. Chemie Int. Ed.*, 2012, **51**, 6131–6135.
21 H. Guo, A. Wu, Y. Xie, H. Yan, D. Wang, L. Wang and C. Tian, *J. Mater. Chem. A*, 2021, **9**, 8620–8629.
22 C. Bai, S. Wei, D. Deng, X. Lin, M. Zheng and Q. Dong, *J. Mater. Chem. A*, 2017, **5**, 9533–9536.
23 W. Xia, R. Zou, L. An, D. Xia and S. Guo, *Energy Environ. Sci.*, 2015, **8**, 568–576.
24 J. Liu, J. Wang, B. Zhang, Y. Ruan, H. Wan, X. Ji, K. Xu, D. Zha, L. Miao and J. Jiang, *J. Mater. Chem. A*, 2018, **6**, 2067–2072.
25 Q. Zhou, T.-T. Li, J. Qian, Y. Hu, F. Guo and Y.-Q. Zheng, *J. Mater. Chem. A*, 2018, **6**, 14431–14439.
26 Z. Liu, H. Tan, D. Liu, X. Liu, J. Xin, J. Xie, M. Zhao, L. Song, L. Dai and H. Liu, *Adv. Sci.*, 2019, **6**, 1801829.
27 X. Wu, J. Li, Y. Li and Z. Wen, *Chem. Eng. J.*, 2021, **409**, 128161.
28 L. Tian, Z. Li, X. Xu and C. Zhang, *J. Mater. Chem. A*, 2021, **9**, 13459–13470.
29 L. Yang, R. Liu and L. Jiao, *Adv. Funct. Mater.* 2020, **30**, 1909618.
30 Y. Tan, H. Wang, P. Liu, Y. Shen, C. Cheng, A. Hirata, T. Fujita, Z. Tang and M. Chen, *Energy Environ. Sci.*, 2016, **9**, 2257–2261.
31 J. Wang, G. Lv and C. Wang, *Appl. Surf. Sci.*, 2021, **570**, 151182.
32 Y. Sun, Y. Zhou, Y. Zhu, Y. Shen and A. Xie, *ACS Sustain. Chem. Eng.*, 2019, **7**, 9153–9163.
33 J. Liu, C. Wang, H. Sun, H. Wang, F. Rong, L. He, Y. Lou, S. Zhang, Z. Zhang and M. Du, *Appl. Catal. B Environ.*, 2020, **279**, 119407.
34 M. Fang, G. Dong, R. Wei and J. C. Ho, *Adv. Energy Mater.* 2017, **7**, 1700559.
35 L. B. Staal, S. S. Charan Pushparaj, C. Forano, V. Prevot, D. B. Ravnsbæk, M. Bjerring and U. G. Nielsen, *J. Mater. Chem. A*, 2017, **5**, 21795–21806.
36 Y. Zhang, B. Cui, Z. Qin, H. Lin and J. Li, *Nanoscale*, 2013, **5**, 6826.
37 W. S. Khan, C. Cao, Z. Ali, F. K. Butt, N. Ahmad Niaz, A. Baig, R. ud Din, M. H. Farooq, F. Wang and Q. ul Ain, *Mater. Lett.*, 2011, **65**, 2127–2129.
38 F. Jiao, J. Wang, Y. Lin, J. Li, X. Jing and Y. Gong, *Appl. Surf. Sci.*, 2021, **553**, 149440.
39 S. Podila, H. Driss, S. F. Zaman, A. M. Ali, A. A. Al-Zahrani, M. A. Daous and L. A. Petrov, *Int. J. Hydrogen Energy*, 2020, **45**, 873–890.
40 R. Adalati, A. Kumar, M. Sharma, P. Tiwari and R. Chandra, *Appl. Phys. Lett.* 2020, **117**, 123904.
41 M. Moloudi, A. Noori, M. S. Rahmanifar, Y. Shabangoli, M. F. El-Kady, N. B. Mohamed, R. B. Kaner and M. F. Mousavi, *Adv. Energy Mater.*, 2023, **13**, 2203002.

42 J. Jiang, P. Yan, Y. Zhou, Z. Cheng, X. Cui, Y. Ge and Q. Xu, *Adv. Energy Mater.*, 2020, **10**, 2002214.

43 Y. Xi, B. Dong, Y. Dong, N. Mao, L. Ding, L. Shi, R. Gao, W. Liu, G. Su and L. Cao, *Chem. Mater.*, 2016, **28**, 1355–1362.

44 Y. Wen, J. Qi, P. Wei, X. Kang and X. Li, *J. Mater. Chem. A*, 2021, **9**, 10260–10269.

45 K. R. Yoon, K. Shin, J. Park, S.-H. Cho, C. Kim, J.-W. Jung, J. Y. Cheong, H. R. Byon, H. M. Lee and I.-D. Kim, *ACS Nano*, 2018, **12**, 128–139.

46 C. T. Cao, S.-W. Kim, H. J. Kim, R. Purbia, S. H. Kim, D. Kim, K. J. Choi, H. Park and J. M. Baik, *Nano Energy*, 2022, **96**, 107117.

47 B. Zhang, H. Luo, B. Ai, Q. Gou, J. Deng, J. Wang, Y. Zheng, J. Xiao and M. Li, *Small*, 2023, **19**, 2205431.

48 Y. Gao, D. Zheng, Q. Li, W. Xiao, T. Ma, Y. Fu, Z. Wu and L. Wang, *Adv. Funct. Mater.*, 2022, **32**, 2203206.

49 T. L. L. Doan, D. T. Tran, D. C. Nguyen, D. H. Kim, N. H. Kim and J. H. Lee, *Adv. Funct. Mater.*, 2021, **31**, 2007822.

50 J. Yu and J. Kim, *Chemosphere*, 2022, **287**, 132168.

51 Z. Xu, Y. Jiang, J.-L. Chen and R. Y.-Y. Lin, *ACS Appl. Mater. Interfaces*, 2023, **15**, 16702–16713.

52 P. P. Dhakal, U. N. Pan, D. R. Paudel, M. R. Kandel, N. H. Kim and J. H. Lee, *Mater. Today Nano*, 2022, **20**, 100272.

53 W.-H. Huang, X.-M. Li, X.-F. Yang, H.-B. Zhang, F. Wang and J. Zhang, *Chem. Commun.*, 2021, **57**, 4847–4850.

54 Y. Wu, G.-D. Li, Y. Liu, L. Yang, X. Lian, T. Asefa and X. Zou, *Adv. Funct. Mater.*, 2016, **26**, 4839–4847.

55 D. C. Nguyen, T. L. L. Doan, S. Prabhakaran, D. H. Kim, N. H. Kim and J. H. Lee, *Nano Energy*, 2021, **89**, 106420.

56 B. K. Kang, S. Y. Im, J. Lee, S. H. Kwag, S. Bin Kwon, S. Tiruneh, M.-J. Kim, J. H. Kim, W. S. Yang, B. Lim and D. H. Yoon, *Nano Res.*, 2019, **12**, 1605–1611.

57 A. J. Addie, M. A. Mohammed and R. A. Ismail, *Mater. Sci. Semicond. Process.*, 2022, **145**, 106664.

58 T. Varga, G. Ballai, L. Vásárhelyi, H. Haspel, Á. Kukovecz and Z. Kónya, *Appl. Catal. B Environ.*, 2018, **237**, 826–834.

59 C. Liu, G. Bai, X. Tong, Y. Wang, B. Lv, N. Yang and X.-Y. Guo, *Electrochem. commun.*, 2019, **98**, 87–91.

60 M. Chen, D. Liu, L. Qiao, P. Zhou, J. Feng, K. W. Ng, Q. Liu, S. Wang and H. Pan, *Chem. Eng. J.*, 2023, **461**, 141939.

61 Y.-H. Wang, S. Zheng, W.-M. Yang, R.-Y. Zhou, Q.-F. He, P. Radjenovic, J.-C. Dong, S. Li, J. Zheng, Z.-L. Yang, G. Attard, F. Pan, Z.-Q. Tian and J.-F. Li, *Nature*, 2021, **600**, 81–85.

62 T. Begildayeva, J. Theerthagiri, S. J. Lee, Y. Yu and M. Y. Choi, *Small*, 2022, **18**, 2204309.

63 J. Zhang, W. He, H. B. Aiyappa, T. Quast, S. Dieckhöfer, D. Öhl, J. R. C. Junqueira, Y. Chen, J. Masa and W. Schuhmann, *Adv. Mater. Interfaces*, 2021, **8**, 2100041.